

Chiral Weyl Pockets and Fermi Surface Topology of the Weyl Semimetal TaAs

F. Arnold,¹ M. Naumann,¹ S.-C. Wu,¹ Y. Sun,¹ M. Schmidt,¹ H. Borrmann,¹ C. Felser,¹ B. Yan,^{1,2} and E. Hassinger^{1,3,*}

¹Max Planck Institute for Chemical Physics of Solids, 01187 Dresden, Germany

²Max Planck Institute for Physics of Complex Systems, 01187 Dresden, Germany

³Physik-Department, Technische Universität München, 85748 Garching, Germany

(Received 29 March 2016; revised manuscript received 9 September 2016; published 28 September 2016)

Tantalum arsenide is a member of the noncentrosymmetric monpnictides, which are putative Weyl semimetals. In these materials, three-dimensional chiral massless quasiparticles, the so-called Weyl fermions, are predicted to induce novel quantum mechanical phenomena, such as the chiral anomaly and topological surface states. However, their chirality is only well defined if the Fermi level is close enough to the Weyl points that separate Fermi surface pockets of opposite chirality exist. In this Letter, we present the bulk Fermi surface topology of high quality single crystals of TaAs, as determined by angle-dependent Shubnikov–de Haas and de Haas–van Alphen measurements combined with *ab initio* band-structure calculations. Quantum oscillations originating from three different types of Fermi surface pockets were found in magnetization, magnetic torque, and magnetoresistance measurements performed in magnetic fields up to 14 T and temperatures down to 1.8 K. Of these Fermi pockets, two are pairs of topologically nontrivial electron pockets around the Weyl points and one is a trivial hole pocket. Unlike the other members of the noncentrosymmetric monpnictides, TaAs is the first Weyl semimetal candidate with the Fermi energy sufficiently close to both types of Weyl points to generate chiral quasiparticles at the Fermi surface.

DOI: 10.1103/PhysRevLett.117.146401

The noncentrosymmetric monophosphides (TaP, NbP) and monoarsenides (TaAs, NbAs) are members of a new class of topological materials, the Weyl semimetals. These are thought to host new exotic quantum mechanical phenomena such as topological surface states [1] and the chiral transport anomaly [2,3] due to the presence of three-dimensional chiral massless Weyl fermions [4,5]. Electrons in semimetals behave as Weyl fermions if the bands disperse linearly in reciprocal space near three dimensional band crossing points (Weyl nodes), and the spin is locked to the wave vector \mathbf{k} such that the chirality is given by the sign of $\boldsymbol{\sigma} \cdot \mathbf{k}$, where $\boldsymbol{\sigma}_i$ are the Pauli matrices. This can be realized in semimetals with strong spin-orbit coupling (SOC) and broken inversion or time-reversal symmetry, which induces pairs of Weyl nodes of opposite chirality [6,7].

Probes sensitive to the Fermi surface (FS), such as specific heat, magnetization, and electrical transport are expected to show unconventional behavior related to massless chiral fermions only if the Fermi energy E_F is close to the Weyl points. More precisely, this window of energies is defined by the existence of separate Fermi pockets around each Weyl point (Weyl pockets), giving rise to quasiparticles of well-defined chirality. Detuning the Fermi energy beyond this range leads to the merging of neighboring Weyl pockets and cancellation of the associated Berry flux and chirality. Thus, a precise knowledge of the band structure and E_F is needed in order to attribute observed anomalous quantum phenomena to chiral Weyl fermions.

Early angle-resolved photo emission spectroscopy (ARPES) studies observed Fermi arcs on the sample surface of TaP and TaAs and linearly dispersing bands in the bulk, proving the existence of two sets of Weyl nodes ($W1$ and $W2$) in these materials [8–10]. However, due to the limited energy resolution of ARPES, the precise location of E_F with respect to the Weyl points and the resulting FS topology remained an open question. Recently Klotz *et al.* and Arnold *et al.* reported on the bulk FS topology of NbP and TaP, respectively [11,12]. By combined quantum oscillation studies and band-structure calculations, it was shown that E_F in both materials is well outside the range for observing chiral Weyl fermions, and the FS consists only of topologically trivial pockets.

Here we present the first demonstration of Fermi-level Weyl fermions of opposite chirality in a monoarsenide or monophosphide, by showing that in as-grown crystals of TaAs, E_F is within the window of separate FS pockets around each Weyl point. A full angular dependence study of the de Haas–van Alphen (dHvA) and Shubnikov–de Haas (SdH) effect of high quality single crystals of TaAs was performed by means of magnetization, magnetic torque, and electrical transport measurements. Unlike previous studies [13,14], we obtain a unique solution for the FS topology by considering hitherto undiscovered quantum oscillation frequencies of the minor Weyl and hole pockets, which allow us to locate the E_F with millielectronvolt precision.

The band structure of TaAs was calculated using the Vienna *ab initio* simulation package [15] and modified Becke-Johnson exchange potential [16,17] (see Fig. 1). FSs were interpolated using maximally localized Wannier functions [18] in dense k grids ($300 \times 300 \times 300$ points over the entire Brillouin zone). In the absence of SOC, the spin degenerate valence and conduction bands cross each other along four so-called “nodal rings.” These rings lie in the (100) and (010) mirror planes [see dashed rings in Fig. 3(b)] [6]. SOC lifts the spin degeneracy and gaps out the nodal ring except for the band crossings at the Weyl points. Here, the oppositely spin-polarized valence and conduction band cross [6,7]. Along each nodal ring, two types of Weyl points exist. One pair of Weyl points is located at $k_z = 0$ and another two pairs lie at $k_z = \pm\pi/c$. These Weyl points are labeled $W1$ and $W2$, respectively, and the $W1$ Weyl points reside at slightly lower energy compared to $W2$. As E_F does generally not line up with the Weyl points, FS pockets enclosing individual or pairs of Weyl points will arise. In the former case the opposite chirality of the quasiparticles within a pair of Weyl pockets is conserved. The gray shaded bands in Fig. 1 indicate the energy range for which this is expected. In the latter case, however, the total Berry flux through the FS is zero and the quasiparticles are nonchiral. Depending on E_F , Weyl pockets coexist and merge with topologically trivial electron and hole pockets, which originate from local minima or maxima of either the valence or conduction band along the nodal ring.

Crystals of TaAs were grown by chemical vapor transport starting from microcrystalline powder synthesized by

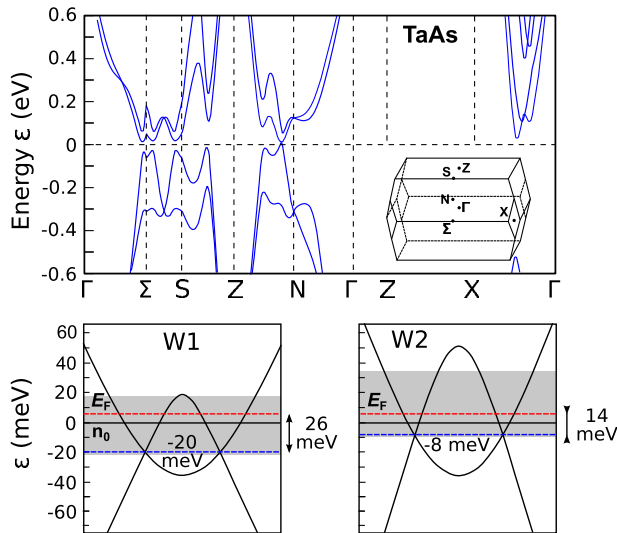


FIG. 1. Top: *ab initio* band structure of TaAs. Bottom: Scheme of the bands close to the Fermi energy along the line connecting the Weyl nodes. n_0 marks the charge neutral point, E_F the Fermi energy as determined by quantum oscillations. The gray shaded area corresponds to the energy window in which separate Fermi surface pockets of opposite chirality exist.

reacting tantalum (Chempur 99.9%) and arsenic (Alfa Aesar 99.9999%) [12,19]. The resulting crystals showed a residual resistivity ratio of 10 (see Fig. S3 of the Supplemental Material [20]). Their crystalline structure, lattice constants, and alignment were confirmed using x-ray diffraction techniques [20].

Quantum oscillations (QOs), the dHvA and SdH effect, are a powerful tool to reconstruct the FS topology in metals and arise due to the $1/B$ -periodic depopulation of Landau levels (LLs) at E_F with increasing magnetic field [21]. Their frequency $F = \hbar/2\pi eA$ is related to the extremal FS cross section A normal to the magnetic field, and can be used to reconstruct the FS topology of metals [22,23]. The magnetization and dHvA oscillations of TaAs along all major axes and selected angles in between were measured in a Quantum Design (QD) 7T SQUID-VSM at temperatures between 2 and 20 K [see Fig. 2(a) and Fig. S6 of the Supplemental Material [20]]. Angle-dependent SdH and dHvA measurements were performed at 1.8 K in a 14 T QD Physical-Property Measurement System (PPMS) using a QD rotator probe and TqMag piezoelectric torque cantilevers [24]. Further details and raw resistance and magnetic torque data for magnetic fields applied within the (100) and (110) plane can be found in the Supplemental Material [20].

Magnetization data and their background-subtracted dHvA oscillations for $B \parallel [100]$, $[110]$ and $[001]$ at 2 K are shown in Fig. 2(a). As can be seen, TaAs shows a diamagnetic magnetization. Strong QOs are visible in all three directions. This is in contrast to NbP and TaP, where quantum oscillations are weak for magnetic fields applied in the (001) plane [11,12]. The inset of Fig. 2(a) shows the background-subtracted dHvA oscillations plotted against F/B . The observed low frequencies are indicative of very small FS pockets as are typical for semimetals with low charge carrier densities. The frequency of $F_\alpha = 7.0$ T for $B \parallel [001]$ agrees well with previous reports by other groups [13,14,25]. In addition, we find a steplike magnetization feature along the $[100]$ and $[110]$ direction starting at $F/B = 1$ or, equivalently, 1.4 and 1.9 T, which is attributed to the quantum limit of the lowest frequency F_β . At this step the dominant frequency vanishes and a second larger frequency F_γ becomes visible up to 3 T (4 T) for $B \parallel [100]$ ($B \parallel [110]$) [20].

The detailed angular dependence of the QO frequencies was determined by combined electrical transport [see, e.g., Fig. 2(b)] and magnetic torque measurements. Fourier transforms of multiple field windows and measurement techniques were correlated to exclude higher harmonics and to produce the angular dependence shown in Fig. 3(a). Table I contains a summary of all QO frequencies along the major axes.

We have successfully reconstructed the FS topology by tuning E_F to +6 meV in our band structure (Fig. 1). We can fit our measured QO frequencies with the predicted

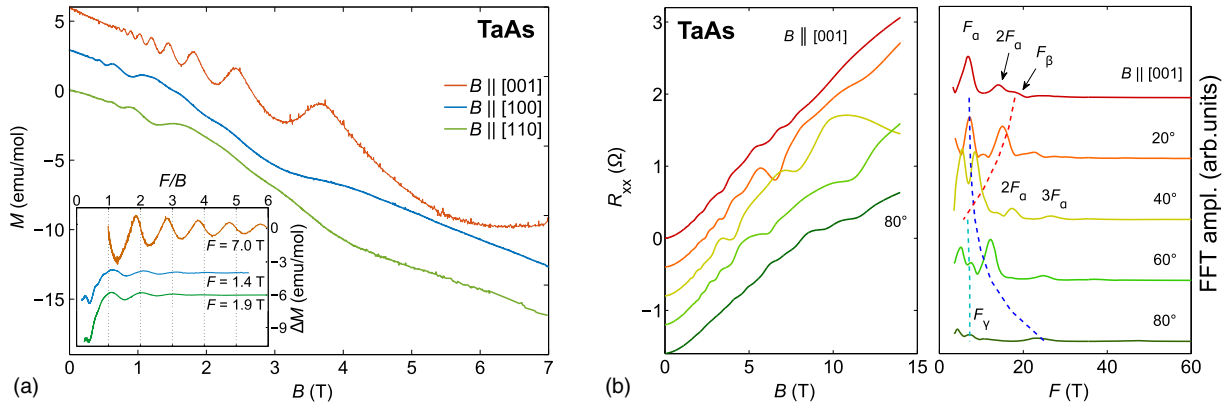


FIG. 2. (a) Magnetic field dependence of the magnetization at 2 K. The inset shows the de Haas–van Alphen oscillations plotted over the inverse magnetic field normalized by the lowest quantum oscillation frequency. A linear background fitted to the low field magnetization was subtracted. Curves are offset for clarity. (b) Left panel: transverse magnetoresistance for magnetic fields applied within the (100) plane in steps of 20° measured at 2 K (data have been offset by 0.4Ω each for clarity). Right panel: corresponding Fourier transformations of the background subtracted Shubnikov-de Haas signals over a magnetic field range of 1 to 14 T. The dashed lines are guides to the eye showing the angular dependence of F_α , F_β , and F_γ .

angular dependence of the extremal orbit size [Fig. 3(a)]. This energy is well within the energy window for observing chiral FS pockets (see Fig. 1) and the FS is described by three Weyl pocket pairs, one $W1$ and two $W2$ pairs. These coexist with two trivial hole pockets, $H1$, aligned along the nodal ring [see Figs. 3(b) and 3(c)]. Crucially, a unique solution of the FS topology was only achieved by including all three QO frequency branches. This way it was possible to eliminate alternative topologies deep in the hole and electron doped regime, which give rise to a similar $1/\cos(\theta)$ dependence of the dominant $F_\alpha = 7$ T frequency (see Fig. S10 of the Supplemental Material [20]). Based on the energy dependence of the FS topology and uncertainty of our QO frequencies (see Fig. S9 of the Supplemental Material [20]), we estimate a E_F uncertainty of 1 meV.

The banana-shaped electron $W1$ pockets at the zone boundary, which are aligned parallel to the [001] axis, give

rise to an inverse $\cos(\theta)$ -like angular dependence of the F_α branch [continuous blue lines in Fig. 3(a)] when the magnetic field is tilted away from the [001] axis. Experimental and theoretical values of the extremal orbit size can be found in Table I. The tetragonal crystal symmetry and consequential 90° repetition of the FS pockets around the [001] axis causes a splitting of all frequency branches away from the [001]-axis. The chiral character of this pocket induces a phase shift close to π between F_α and the topologically trivial F_β in the inset of Fig. 2(a).

The $W2$ pockets on the other hand are rather isotropic spheres. Their angular dependence is split into four branches due to their off-planar position and low symmetry. The corresponding frequency F_γ [dashed blue lines in Fig. 3(a)] is almost independent of the magnetic field direction, in agreement with our experimental results [horizontally aligned black data points].

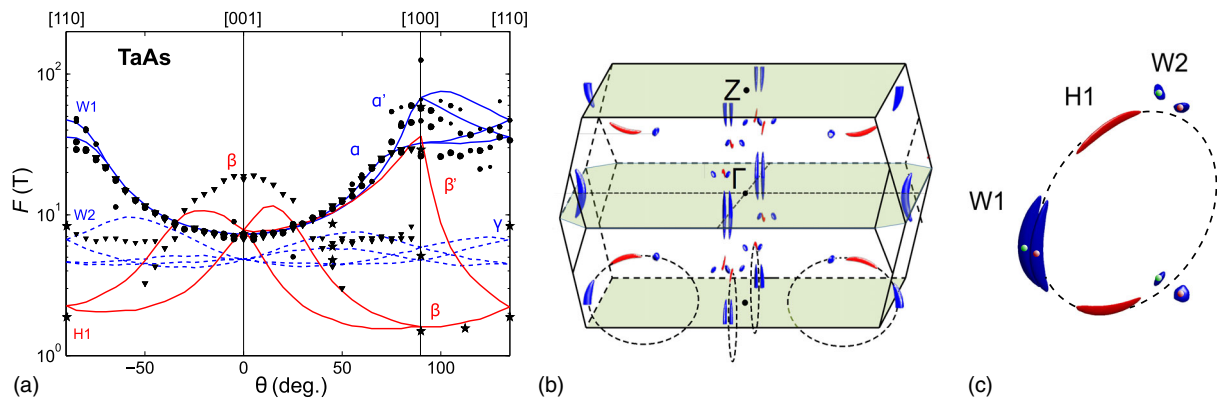


FIG. 3. (a) Angular dependence of the quantum oscillation frequencies F of TaAs for magnetic fields applied within the (100), (110), and (001) plane. Black triangles, dots, and stars represent frequencies determined from electrical transport, magnetic torque, and magnetization, respectively. The solid and dashed lines show the theoretical angular dependence according to the *ab initio* band structure at a Fermi energy of +6 meV. (b) and (c) First Brillouin zone and Fermi surface topology of TaAs according to the angular dependence in graph (a). The dashed rings show the nodal lines as explained in the text.

TABLE I. Experimental and calculated quantum oscillation frequencies F and effective cyclotron masses m^* for different magnetic field orientations at $E_F = +6$ meV. m_0 is the free electron mass.

Pocket	Orbit	Experiment		Calculation	
		F (T)	$m^*(m_0)$	F (T)	$m^*(m_0)$
W1	α $B \parallel [001]$	7.0(5)	0.057(3)	7.25	0.065
	α $B \parallel [100]$	29(1)	...	32	0.24
	α' $B \parallel [100]$	59(3)	...	68	0.68
W2	γ $B \parallel [100]$	5.4(3)	0.105(3)	5.3	0.076
	γ $B \parallel [110]$	8.2(1)	...	5.5	0.082
H1	β $B \parallel [001]$	19.0(5)	...	7.77	0.17
	β $B \parallel [100]$	1.4(2)	0.010(1)	1.59	0.024
	β $B \parallel [110]$	1.9(2)	0.020(5)	2.20	0.035

The $H1$ hole pockets give rise to the F_β branch [red lines in Fig. 3(a)]. Experimentally, we observe a continuous decrease of F_β from 19 to $F_\beta = 1.4$ and 1.9 T when the magnetic field is tilted away from the [001] axis [black triangles close to [001] in Fig. 3(a)]. This is indicative of a strongly anisotropic ellipsoidal pocket aligned almost parallel to the [100] axes. The calculations, on the other hand, show an initial increase, peaking around 12° , towards the [100] axis. This initial increase is due to the non-horizontal alignment of the hole pocket in the Brillouin zone. The observed discrepancy between the experimental drop and theoretical increase of F_β [Fig. 3(a)] can be explained by minor deformations of the ellipsoidal pocket. Because of its large anisotropy and slightly off-horizontal alignment, a weak bend or minor convexities on the surface of the pocket can stabilize a large orbit for magnetic fields along the [001] axis. Such fine structures are, however, beyond the accuracy of our DFT calculations.

As we saw in the magnetization data, it is the $H1$ pocket which reaches its quantum limit above 2 T for magnetic fields within the (001) plane. The magnetization steps at $F_\beta/B = 1$ along the [100] and [110] axes correspond to the second last LL crossing E_F . Beyond this field only the $n = 0$ LL remains occupied. The quantum limit field scales with the QO frequency and $F_\beta[110] \approx \sqrt{2}F_\beta[100]$, as expected for a quasi-two-dimensional FS aligned parallel to the [100] axis. Thus, no quantum limit signature is expected in the magnetic field range up to 7 T for $B \parallel c$. As the electrical transport is dominated by the larger $W1$ and $W2$ pockets, which are still described by multiple LLs in this field range, no clear transport anomalies are observed.

Charge carrier cyclotron masses of all three pockets have been determined by fits of the Lifshitz-Kosevich temperature reduction term to the temperature dependence of the quantum oscillation amplitude (see Fig. 4) [26,27] and are given in Table I. The small cyclotron masses, ranging between $0.01m_0$ for $H1$ and $0.1m_0$ for $W2$, are in agreement with our band-structure calculations [20]. The finite cyclotron masses of the $W1$ and $W2$ electrons are an indication

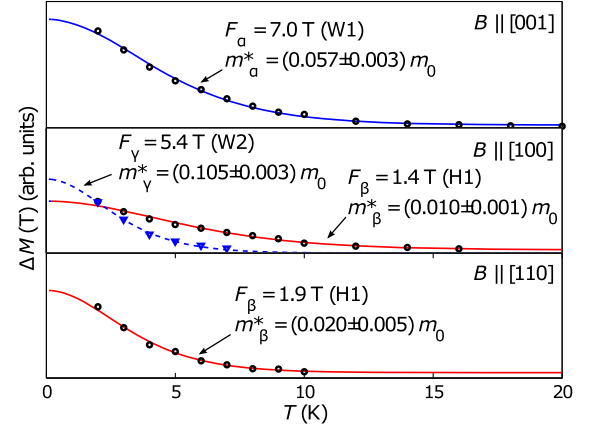


FIG. 4. Temperature dependences of the de Haas-van Alphen oscillation amplitude as determined from magnetization measurements in the magnetic field interval of 1 to 7 T along the high symmetry axes. Lines are fits to the Lifshitz-Kosevich temperature reduction term $\tilde{M} \propto x/\sinh(x)$ with $x = \pi^2 m^* k_B T / \mu_B B$ [21,26,27].

for the mismatch between E_F and both Weyl points. For linearly dispersing bands the usual definition of $m^* = \hbar/2\pi(\partial A/\partial E_F)$ [28] leads only to a vanishing mass at the Weyl point and increases linearly with energy otherwise.

As E_F lies 6 meV above the charge neutral point (see Fig. 1) the system is slightly electron doped. From the volumina of the electron and hole FS, we obtain a theoretical electron doping of $3.5 \times 10^{18} \text{ cm}^{-3}$. This compares reasonably well to an electron doping of $(1.0 \pm 0.5) \times 10^{19} \text{ cm}^{-3}$, which was determined from Hall resistivity by applying a single-band model (see Fig S4 of the Supplemental Material [20]). Contrary to an ideal compensated semimetal the observed doping might indicate slight deviations from a defect free stoichiometric crystal. However, different growth conditions do not seem to affect the QO frequencies of TaAs and thus its doping level and E_F [13,14,25].

A Dingle analysis of the $W1$ and $H1$ dHvA oscillations (see Fig. S7 of the Supplemental Material [20]) reveals scattering times of $\tau(W1) = 3.8 \times 10^{-13}$ and $\tau(H1) = 1.1 \times 10^{-13}$ s or, equivalently, Dingle temperatures of $T_D(W1) = 3.2$ and $T_D(H1) = 11$ K, respectively [29]. Taking into account the theoretical Fermi velocity of both pockets $v_F(W1) = 296 \times 10^3$ and $v_F(H1) = 755 \times 10^3$ m/s we obtain a charge carrier mean-free path of $l = (95 \pm 15)$ nm. The corresponding dHvA electron and hole mobilities $\mu = \tau e/m^*$ are $\mu_e = 1.2 \times 10^4 \text{ cm}^2/\text{V s} = 1.2 \text{ T}^{-1}$ and $\mu_h = 1.9 \times 10^4 \text{ cm}^2/\text{V s} = 1.9 \text{ T}^{-1}$.

In summary, we observed quantum oscillations from three types of FS pockets in TaAs. By considering the angular dependence of all observed QO frequency branches, we were able to obtain a unique solution for the FS topology based on additional DFT calculations. The FS consists of three pairs of topological Weyl pockets and

two trivial hole pockets aligned along each nodal ring of the tetragonal Brillouin zone. In TaAs, E_F is such that each Weyl point is surrounded by a distinct FS pocket of well-defined chirality and π -Berry phase. Compared to the other members of the noncentrosymmetric monopnictides [11,12], TaAs is thus the first Weyl semimetal with confirmed chiral quasiparticles at E_F . Therefore, TaAs is a prime candidate for the observation of chiral effects such as the Adler-Bell-Jackiw anomaly.

The authors would like to acknowledge the Max-Planck Society for their support of the MPRG as well as Kamran Behnia, Jens Bardarson, Michael Nicklas, and Andy Mackenzie for stimulating and fruitful discussions.

*Corresponding author.

elena.hassinger@cpfs.mpg.de

- [1] X. Wan, A. M. Turner, A. Vishwanath, and S. Y. Savrasov, *Phys. Rev. B* **83**, 205101 (2011).
- [2] S. L. Adler, *Phys. Rev.* **177**, 2426 (1969).
- [3] J. Bell and R. Jackiw, *Nuovo Cimento A* **60**, 47 (1969).
- [4] H. Weyl, *Z. Phys.* **56**, 330 (1929).
- [5] G. Volovik, *Lect. Notes Phys.* **870**, 343 (2013).
- [6] H. Weng, C. Fang, Z. Fang, B. A. Bernevig, and X. Dai, *Phys. Rev. X* **5**, 011029 (2015).
- [7] S.-M. Huang, S. Xu, I. Belopolski, C. Lee, G. Chang, B. Wang, N. Alidoust, G. Bian, M. Neupane, C. Zhang *et al.*, *Nat. Commun.* **6**, 7373 (2015).
- [8] B. Lv, H. Weng, B. Fu, X. Wang, H. Miao, J. Ma, P. Richard, X. Huang, L. Zhao, G. Chen *et al.*, *Phys. Rev. X* **5**, 031013 (2015).
- [9] S.-Y. Xu, I. Belopolski, N. Alidoust, M. Neupane, G. Bian, C. Zhang, R. Ankar, G. Chang, Z. Yuan, C.-C. Lee *et al.*, *Science* **349**, 613 (2015).
- [10] L. Yang, Z. Liu, Y. Sun, H. Peng, H. Yang, T. Zhang, B. Zhou, Y. Zhang, Y. Guo, M. Rahn *et al.*, *Nat. Phys.* **11**, 728 (2015).
- [11] J. Klotz, S.-C. Wu, C. Shekhar, Y. Sun, M. Schmidt, M. Nicklas, M. Baenitz, M. Uhlarz, J. Wosnitzer, C. Felser, and B. Yan, *Phys. Rev. B* **93**, 121105(R) (2016).
- [12] F. Arnold, C. Shekhar, S.-C. Wu, Y. Sun, R. D. dos Reis, N. Kumar, M. Naumann, M. O. Ajeesh, M. Schmidt, A. G. Grushin *et al.*, *Nat. Commun.* **7**, 11615 (2016).
- [13] C. Zhang, Z. Yuan, S. Xu, Z. Li, B. Tong, M. Z. Hasan, J. Wang, C. Zhang, and S. Jia, [arXiv:1502.00251](https://arxiv.org/abs/1502.00251).
- [14] X. Huang, L. Zhao, Y. Long, P. Wang, D. Chen, Z. Yang, H. Liang, M. Xue, H. Weng, Z. Fang *et al.*, *Phys. Rev. X* **5**, 031023 (2015).
- [15] G. Kresse and J. Furthmüller, *Phys. Rev. B* **54**, 11169 (1996).
- [16] A. Becke and E. Johnson, *J. Chem. Phys.* **124**, 221101 (2006).
- [17] F. Tran and P. Blaha, *Phys. Rev. Lett.* **102**, 226401 (2009).
- [18] A. Mostofi, *Comput. Phys. Commun.* **178**, 685 (2008).
- [19] J. Martin and R. Gruehn, *Z. Kristallogr.* **182**, 180 (1988).
- [20] See Supplemental Material at <http://link.aps.org/supplemental/10.1103/PhysRevLett.117.146401> for raw resistance and magnetic torque data as well as detailed analyses of the Hall effect, cyclotron masses, scattering times, angular dependence of the quantum oscillation frequencies and Fermi surface topology.
- [21] D. Shoenberg, *Magnetic Oscillations in Metals* (Cambridge University Press, Cambridge, England, 2009).
- [22] L. Onsager, *Philos. Mag.* **43**, 1006 (1952).
- [23] P. E. C. Ashby and J. P. Carbotte, *Eur. Phys. J. B* **87**, 92 (2014).
- [24] C. Rossel, P. Bauer, D. Zech, J. Hofer, M. Willemin, and H. Keller, *J. Appl. Phys.* **79**, 8166 (1996).
- [25] C. Zhang, S. Xu, I. Belopolski, Z. Yuan, Z. Lin, B. Tong, G. Bian, N. Alidoust, C. Lee, S. Huang *et al.*, *Nat. Commun.* **7**, 10735 (2016).
- [26] I. Lifshitz and A. Kosevich, *Zh. Eksp. Teor. Fiz.* **29**, 730 (1956) [*Sov. Phys. JETP* **2**, 636 (1956)].
- [27] I. Lifshitz and A. Kosevich, *J. Phys. Chem. Solids* **4**, 1 (1958).
- [28] N. W. Ashcroft and D. N. Mermin, *Solid State Physics* (Brooks/Cole Cengage Learning, Belmont, CA, 1976).
- [29] R. Dingle, *Proc. R. Soc. A* **211**, 517 (1952).